$4f$ occupancy and magnetism of rare-earth atoms adsorbed on metal substrates

Aparajita Singha,[1] Romana Baltic,[1] Fabio Donati,[2,1,3] Christian Wäckerlin,[4] Jan Dreiser,[1,5] Luca Persichetti,[6] Sebastian Stepanow,[6] Pietro Gambardella,[6] Stefano Rusponi,[1] and Harald Brune[1,*]

[1]*Institute of Physics, École Polytechnique Fédérale de Lausanne, Station 3, CH-1015 Lausanne, Switzerland*

[2]*Center for Quantum Nanoscience, Institute for Basic Science (IBS), Seoul 03760, Republic of Korea*

[3]*Department of Physics, Ewha Womans University, Seoul 03760, Republic of Korea*

[4]*Nanoscale Materials Science, Empa, Swiss Federal Laboratories for Materials Science and Technology, 8600 Dübendorf, Switzerland*

[5]*Swiss Light Source, Paul Scherrer Institute, CH-5232 Villigen PSI, Switzerland*

[6]*Department of Materials, ETH Zürich, Hönggerbergring 64, CH-8093 Zürich, Switzerland*

(Received 27 April 2017; revised manuscript received 8 November 2017; published 13 December 2017)

We report x-ray absorption spectroscopy and x-ray magnetic circular dichroism measurements as well as multiplet calculations for Dy, Ho, Er, and Tm atoms adsorbed on Pt(111), Cu(111), Ag(100), and Ag(111). In the gas phase, all four elements are divalent and we label their $4f$ occupancy as $4f^n$. Upon surface adsorption, and depending on the substrate, the atoms either remain in that state or become trivalent with $4f^{n-1}$ configuration. The trivalent state is realized when the sum of the atomic correction energies ($4f \rightarrow 5d$ promotion energy E_{fd} + intershell coupling energy δE_c) is low and the surface binding energy is large. The latter correlates with a high substrate density of states at the Fermi level. The magnetocrystalline anisotropy of trivalent RE atoms is larger than the one of divalent RE atoms. We ascribe this to the significantly smaller covalent radius of the trivalent state compared to the divalent one for a given RE element. For a given valency of the RE atom, the anisotropy is determined by the overlap between the *spd* states of the RE and the *d* states of the surface. For all investigated systems, the magnetization curves recorded at 2.5 K show absence of hysteresis indicating that magnetic relaxation is faster than about 10 s.

DOI: 10.1103/PhysRevB.96.224418

I. INTRODUCTION

Surface supported single atoms and small clusters are fascinating quantum spin model systems. Starting with the discovery of giant magnetic anisotropy energy (MAE) in single Co atoms on Pt(111) [1], the understanding of the magnetism of single adatoms has evolved rapidly. The most studied elements having been transition metals (TM) [2–10], the attention is now moving to rare-earth (RE) elements [11–16], culminating in the discovery of magnetic stability in single Ho atoms on MgO(100) thin films [17] and in single Dy atoms on graphene on Ir(111) [18].

Tailoring the magnetic properties of surface supported RE atoms demands optimal control of the energy spectrum of their magnetic quantum levels, which dictate the magnetic ground state, the orientation of the easy axis, and the amount of MAE. Given a rotational axis of symmetry, as it is the case for a purely uniaxial crystal field (CF), the quantum levels can be labeled with $|J, J_z\rangle$, where J_z is the projection of J along the quantization axis z. Depending upon the spatial symmetry and electronic properties of the surrounding environment, degree of hybridization, and charge transfer with the substrate, the $4f$ occupancy, and therefore J, can differ from the free atom value. Yet it remains a good quantum number for an integer $4f$ occupancy. In addition, the interaction with the substrate lifts the degeneracy of the J_z levels thereby inducing the MAE barrier and it also determines whether the ground state will possess the maximum, minimum, or intermediate value of J_z [14].

The gas-phase electronic configuration of the lanthanide atoms that we have investigated here is given by $[\mathrm{Xe}]6s^2 5d^0 4f^n$. It is well known that most of these elements change their $4f$ occupancy in bulk [19–22]. Two distinct configurations have been identified as the most common, namely $[6s6p5d]^2 4f^n$ and $[6s6p5d]^3 4f^{n-1}$ addressed in the literature as divalent and trivalent states, respectively. The nomenclature is based on the occupancy of the $[6s6p5d]$-derived valence band. Although mixed valencies have been reported for several early lanthanides [23–27] and Tm [28], most of the late lanthanides are trivalent in bulk [29,30]. For lower coordinated atoms, such as the ones at surfaces [31–34], in thin films [35], in small clusters [19,36], as well as in surface-adsorbed atoms, the $4f$ occupancy is expected to be different than for bulk. Multiple examples of trivalent states of different REs have been reported for surface-supported low coordinated atoms [11,14,16,17]. As for the divalent state, only Dy atoms on graphene/Ir(111) have been reported so far [18]. What triggers the different $4f$ occupancies in the surface-adsorbed REs has remained largely unexplored. With the rapidly growing interest in magnetism of RE adatoms, a comprehensive study of their $4f$ occupancy on different substrates is very valuable.

Here we investigate the $4f$ occupation and the orientation of the easy magnetization axes of RE atoms adsorbed on metal substrates using x-ray absorption spectroscopy (XAS) and x-ray magnetic circular dichroism (XMCD) for thirteen different adatom-substrate combinations. XAS and XMCD are exquisite techniques that allow element specific detection of the magnetic states [14,37]. The line shape of the XMCD $M_{4,5}$ edges is the fingerprint of the occupancy of the $4f$ levels and therefore it gives access to J of the RE under investigation. In addition, the XMCD sum rules [38,39] and

*harald.brune@epfl.ch

multiplet analysis can be used to estimate the corresponding $\langle J_z \rangle$ values. We chose late lanthanides for their large magnetic moments coming from the parallel alignment of L and S. Additionally, they exhibit larger magnetic anisotropy and have been more intensively studied as model systems for atomic magnetic memories in single ion [40–43] and single atom magnets [17,18]. Among the series of late lanthanides, we investigated Dy, Ho, Er, and Tm as they have been found both in divalent and trivalent states in bulk compounds [44], hence, they represent ideal candidates to explore the interplay between surface binding, $4f$ occupancy, and strength of the crystal field. Our measurements of these atoms adsorbed on different substrates suggest that the trivalent state is achieved in the presence of (a) low atomic correction energies ($4f \rightarrow 5d$ promotion energy E_{fd} + intershell coupling energy δE_c) of the REs and (b) a large binding energy emerging from strong hybridization with the electronic states of the substrate. The latter also induces a stronger CF potential, as demonstrated by our multiplet analysis. In addition, the angular dependence of the magnetic moments and the magnetization curves indicate that the REs exhibit stronger MAE in the presence of stronger RE-substrate binding when they are in their trivalent state. The remainder of this article is organized as follows. Section II contains the experimental and theoretical details, the results on the $4f$ occupation are presented in Sec. III A, the trends of magnetic anisotropy are presented in Sec. III B, and our multiplet analysis highlighting the effect of the CF in determining the quantum level distribution of Er is presented in Sec. III C. We conclude in Sec. IV.

II. EXPERIMENTAL AND THEORETICAL DETAILS

A. Sample preparation

The single crystalline substrates [Pt(111), Cu(111), Ag(100), and Ag(111)] were prepared using several Ar^+ ion sputtering and annealing cycles with specific annealing conditions required for the different crystals [14,17]. Electron-beam evaporators equipped with high purity (99.9%) rods of Dy, Ho, Er, and Tm were used for the deposition of the single atoms. The coverage is given in monolayers (ML) where one ML is defined as one adatom per substrate atom. Note that the covalent radius of the late lanthanides significantly exceeds the one of the TM substrates and the difference increases while moving from $5d$ to $3d$ metals. This implies that the REs cannot form a pseudomorphic monolayer, as observed for Er on Cu(111) [16]. The corresponding packing factor was taken into account for the calibration of the XAS edge of RE islands covering $\approx$50% of the surface area, as determined by the STM [45]. For all low coverage measurements, substrates were kept at 4 K during deposition in order to suppress diffusion and island nucleation. To ensure purity of each sample, (a) the rods were well degassed for several days (until no change in the base pressure was observed after switching on or off the evaporator), (b) depositions were performed at a very low base pressure ($\leqslant 4\times10^{-11}$ mbar), and (c) the cryostat was equipped with a nonevaporable getter to minimize the hydrogen content in the residual gas. To validate our degassing procedure, we repeated the same preparation several times and measured the corresponding XAS and XMCD to ensure that the relative weights of different peaks within M_5 were reproducible. Finally, measurements for each sample lasted no longer than 5 hours to limit the exposure to the residual gas, as the latter can lead to spectral changes in some cases (Appendix E).

B. XAS, XMCD, and magnetization curves

The XAS and XMCD measurements were performed with circularly polarized x-rays in total electron yield (TEY) mode at the EPFL/PSI X-Treme beamline of the Swiss Light Source [46]. All measurements were performed by varying the energy of the incident x-rays within the $M_{4,5}$ absorption edge of the corresponding RE. The absorption spectra were normalized with respect to the total flux of incident x-rays measured using a metal grid. These spectra were further normalized with respect to the absorption pre-edge to compensate TEY variations as a function of angle of incidence. Finally, to isolate the signal of the RE adatoms from the background of the corresponding substrate, XAS of the clean surface were subtracted from the overall XAS signature as described in Ref. [16]. The sum of the absorption from the two circular polarizations provides the XAS while the XMCD is obtained from their difference. All spectra were measured at an external magnetic field of $\mu_0 H = 6.8$ T (unless specified otherwise) at $T = 2.5$ K, and in ultrahigh vacuum ($P_{\text{cryostat}} \leqslant 4\times10^{-11}$ mbar). The magnetic field was collinear with the incident x-rays ($\mu_0 \vec{H} \parallel \vec{k}$). To identify the magnetic easy axis, we rotated the sample around an axis perpendicular to the field and beam, and acquired XAS and XMCD at two incident angles, namely, normal, $\theta = 0^\circ$, and grazing, $\theta = 60^\circ$, where θ defines the angle between $\mu_0 \vec{H}$ (or $\vec{k}$) and the surface normal $\vec{n}$ [46].

The magnetization curves $M(\mu_0 H)$ were recorded by acquiring the maximum XMCD of the M_5 edge as a function of $\mu_0 H$, normalized by the corresponding pre-edge of the XAS signal. Note that, apart from the contribution of the M_4 edge, this signal is proportional to the total magnetic moment per atom. Therefore we normalized the magnetization curves obtained from the two angles of incidence such that their ratio at 6.8 T equals the corresponding ratio of the total moments obtained by applying the sum rules on the XAS and XMCD [38,39]. Field sweep of 0.0125 T s^{-1} and photon flux of 2×10^{10} photon mm^{-2} s^{-1} with a beam size of about 1 mm^2 were used for these measurements.

C. Sum rules

The sum rules relate the XAS and XMCD to the ground-state expectation value of effective spin $\langle S_{\text{eff}} \rangle = 2\langle S_z \rangle + 6\langle T_z \rangle$ and orbital $\langle L_z \rangle$ magnetic moments [38,39]. Here z refers to the field (and beam) axis, $\langle S_z \rangle$ is the spin moment, and $\langle T_z \rangle$ is the magnetic dipole moment. The equations relevant for the evaluation of the orbital and spin of the REs are as follows: $\langle L_z \rangle = 3h_f X_{4,5}/I$ and $\langle S_{\text{eff}} \rangle = 3h_f(5X_5 - 3X_{4,5})/I$, where h_f defines the number of holes in the $4f$ shell, $X_{4,5}$ is the XMCD integrated over the entire $M_{4,5}$ edge, and X_5 is the XMCD integrated only over the M_5 edge [39]. The normalization is done with respect to the unpolarized absorption signal, which is defined as $I = \int_\omega (\mu_0(\omega) + \mu_+(\omega) + \mu_-(\omega))d\omega$, where ω is the incident photon energy and $\mu_+(\omega)$, $\mu_-(\omega)$, and $\mu_0(\omega)$ represent the absorption signals with circular plus,

minus, and linear polarizations, respectively [47]. While the first two components are directly measured, it is impossible to experimentally obtain the last one since it requires the photon vector $\vec{k}$ to be perpendicular to the surface normal $\vec{n}$. For simplicity the following assumption of isotropic absorption is commonly adopted: $\mu_0(\omega) = \frac{1}{2}[\mu_+(\omega) + \mu_-(\omega)]$. We have considered the sum rules with this assumption everywhere except for the estimation of the T_z. For the latter we use multiplet analysis to calculate the relative contribution of $\mu_0(\omega)$ and use the resulting I to precisely determine the magnetic moments of the free ions (Sec. II D).

The projected total angular moment $\langle J_z \rangle$ is expressed as $\langle S_z \rangle + \langle L_z \rangle$. While $\langle L_z \rangle$ can be directly derived by applying the sum rules on the measured spectra, $\langle S_z \rangle$ needs to be extracted from $\langle S_{\text{eff}} \rangle$. For this purpose, we assume that the ratio $\langle T_z \rangle / \langle S_z \rangle$ does not change upon surface adsorption, i.e., it remains the same as in the case of gas-phase atoms [14]. Given this assumption, we first obtain $\langle T_z \rangle_{\text{free}} / \langle S_z \rangle_{\text{free}}$ from the multiplet calculations of the free ions (Sec. II D) and further extract $\langle S_z \rangle$ from the following expression: $\langle S_z \rangle = \langle S_{\text{eff}} \rangle / (2 + 6\frac{\langle T_z \rangle_{\text{free}}}{\langle S_z \rangle_{\text{free}}})$. Here the subscript free denotes values obtained from multiplet calculations for the free ions and $\langle S_{\text{eff}} \rangle$ is obtained by applying the sum rules on the measured spectra.

D. Multiplet calculations

In order to determine the occupation of the 4f levels, we compare the line shape of our experimental spectra with simulated XAS and XMCD of the REs using the MULTIX software [48]. These calculations are performed for both trivalent and divalent forms of the free RE ions, i.e., without any CF, at $\mu_0 H = 6.8$ T and $T = 2.5$ K. This approach works well as a first step since the XAS line shape and, in particular, the position of the maximum of the XMCD of a given RE are mainly determined by the 4f occupancy [30].

For the multiplet calculations, the experimental line broadening due to the finite lifetime of the core-hole state is modeled by convolution with a Gaussian of $\sigma = 0.3$ eV. Note that the MULTIX code relies on the radial functions derived from the corresponding neutral atoms [48]. Therefore the simulation of the free ions necessitates adjustments of all radial function dependent interactions, e.g., the spin-orbit coupling and Coulomb interactions. The spin-orbit coupling of the core levels was scaled in order to match the experimentally observed splittings between the M_4 and M_5 edge (Table I). The Coulomb interaction was scaled such as to reproduce the separations between the multiplet features within the M_5 edge (Table I). The energy axis of all simulated spectra are offset to match the experimental ones.

As discussed earlier in Sec. II C, we need to compute $\langle T_z \rangle$ for the free ion cases. To the best of our knowledge, these values are reported only for the trivalent RE atoms [49]. Since in this work we have encountered both trivalent and divalent states, we employed the multiplet analysis to evaluate $\langle T_z \rangle$ for both types of 4f occupancy for a given RE. We use the spin sum rule to obtain $\langle T_z \rangle$, i.e., $\langle T_z \rangle = (2\langle S_z \rangle - \langle S_{\text{eff}} \rangle)/6$ [38,39]. Here, S_z is the spin moment generated by the MULTIX code for the simulated ground state of the free ion while $\langle S_{\text{eff}} \rangle$ is obtained by applying the sum rules on the simulated spectra (Table I). Note that the estimated $\langle T_z \rangle$ values of the trivalent REs are in very good agreement with the values reported in Ref. [49] (Table VIII).

TABLE I. MULTIX simulation: the Coulomb (CO), spin-orbit coupling for core (SO-core), and for valence (SO-val) states used for the simulations of XAS and XMCD spectra of each free ion of defined 4f occupancy. These are the rescaling factors for the electron-electron Coulomb interaction and spin-orbit coupling, respectively, and are expressed as % of the corresponding Hartree-Fock values. $\langle T_z \rangle$ is the estimated magnetic dipole moment.

Rare earths	4f occupation (number of electrons)	MULTIX parameters			$\langle T_z \rangle$ ($\hbar$)
		CO	SO-val	SO-core	
Dy	$4f^{n-1}(9)$	0.75	0.85	0.95	+0.186
	$4f^{n}(10)$	0.70	0.85	0.97	−0.106
Ho	$4f^{n-1}(10)$	0.90	0.96	0.96	−0.086
	$4f^{n}(11)$	0.80	1.00	1.00	−0.297
Er	$4f^{n-1}(11)$	0.85	0.97	0.97	−0.301
	$4f^{n}(12)$	0.85	1.00	1.00	−0.394
Tm	$4f^{n-1}(12)$	0.85	0.93	0.93	−0.392
	$4f^{n}(13)$	0.85	1.00	1.00	−0.308

Multiplet simulations including the effects of the CF have been performed for Er. The CF was simulated by placing point charges underneath the adsorbed Er atom [48]. Their positions are given relative to the Er atom. The point charge model is simplified compared to the conventional use of the Steven's parameters for describing the CF, and yet it allows us to obtain a quantitative analysis of the magnetic states of surface-supported RE atoms. The x and y coordinates of the ligand charges are derived from the nearest-neighbor positions of the respective substrate while their vertical positions (z) as well as their charges are optimized by applying least square fits (Table VII of Appendix B). Spin-orbit coupling (SO) and Coulomb (CO) parameters were chosen identical to the free ion simulation (Table I).

III. RESULTS AND DISCUSSION

A. 4f occupancy of RE adatoms

Figures 1–4 show the characteristic XAS and XMCD spectra of an ensemble of individual Er, Ho, Dy, and Tm atoms on the different nonmagnetic surfaces. Each RE has the characteristic multiplet structure mostly visible at the M_5 edge, originating from the dipole allowed $3d \rightarrow 4f$ transitions with the following selection rules: $\Delta J = 0, \pm 1$ [50].

(a) Erbium (Er): The XAS line shapes of Er atoms adsorbed on Pt(111), Cu(111), and Ag(100) (Fig. 1) are in very good agreement with the spectra simulated for the $4f^{11}$ configuration as well as with previous reports for trivalent Er [30,51]. The relative amplitudes of the multiplet peaks within the M_5 edge vary with the substrate due to the presence of a different ligand environment. Yet, all the spectra show the main XMCD peak at the same energy. The line shape obtained for adsorption on Ag(111) significantly differs from the rest. In particular, the central XMCD feature is downshifted in energy. This line shape matches well with the spectra simulated for the free ion $4f^{12}$ configuration (bottom panels of Fig. 1), which indicates that Er is in the divalent state on Ag(111). Since

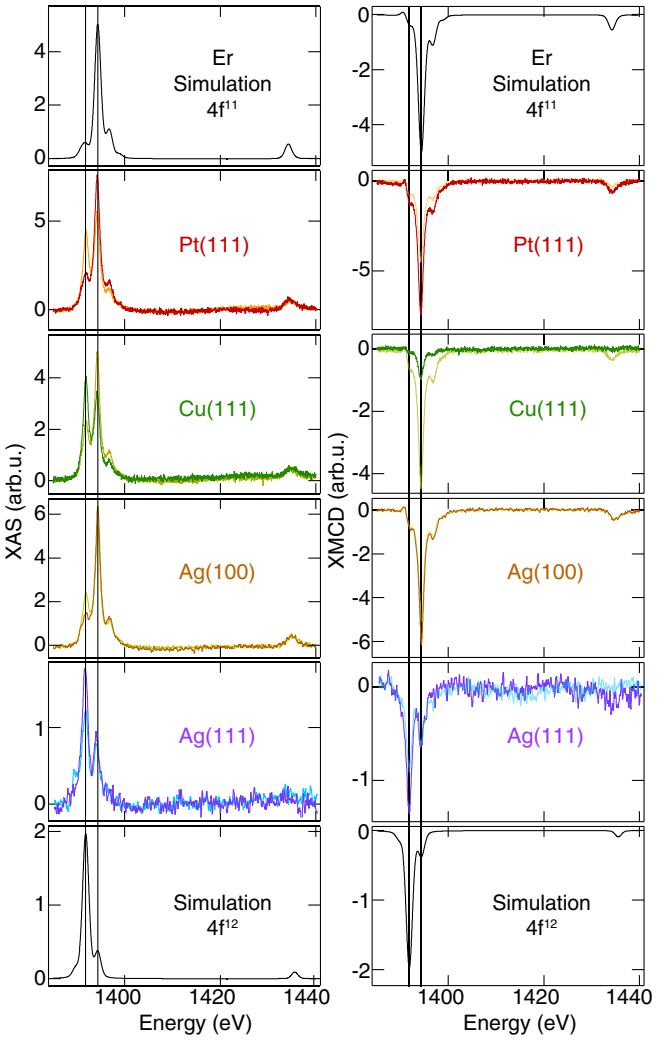

FIG. 1. XAS and XMCD of 0.018, 0.013, 0.014, and 0.005 ML Er on Pt(111), Cu(111), Ag(100), and Ag(111), respectively. All spectra are measured at 6.8 T apart from the ones of Er/Ag(111), which are measured at 5 T. Normal (grazing) incidence spectra are shown in darker (lighter) color. MultiX simulations of the trivalent and divalent state are shown in top and bottom panels for comparison.

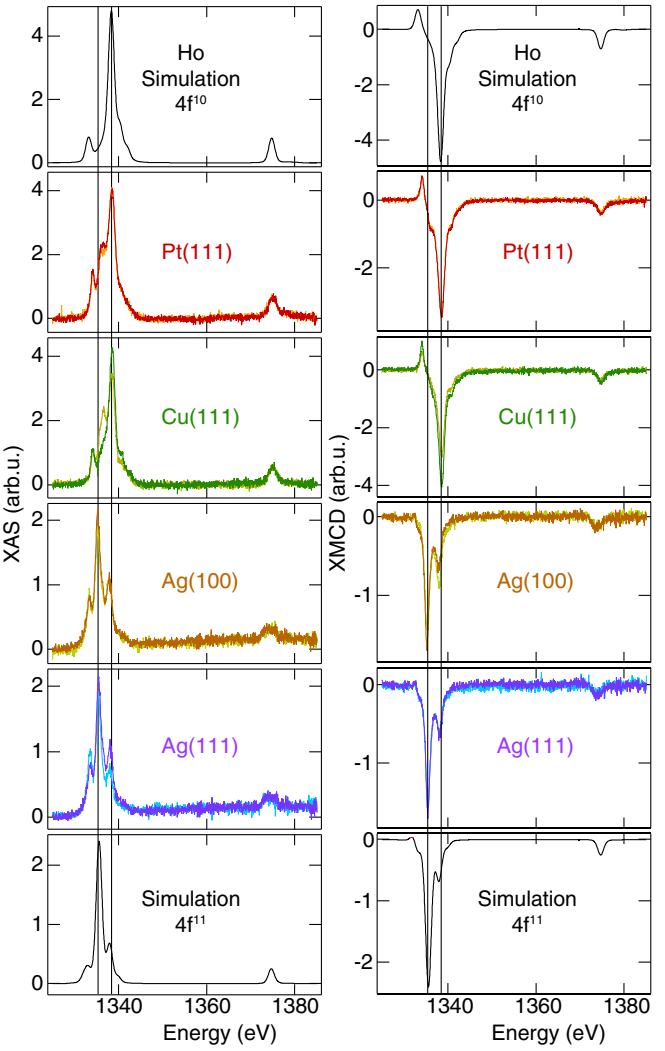

FIG. 2. XAS and XMCD of 0.011, 0.009, 0.006, and 0.005 ML Ho on Pt(111), Cu(111), Ag(100), and Ag(111), respectively. Normal (grazing) incidence spectra are shown in darker (lighter) color. Multiplet simulations of the trivalent and divalent state are shown in top and bottom panels for comparison.

the CF alone cannot account for such a large energy shift, we attribute the observed shift in the central XMCD feature to an overall change in the $4f$ occupancy. This applies to all the RE-substrate combinations discussed hereafter.

(b) Holmium (Ho): The $4f$ occupancy of Ho is identified by comparing the simulated XAS and XMCD spectra with the experimental ones for each substrate. We find a trivalent configuration of Ho, i.e., $4f^{10}$ for adsorption on Pt(111) and Cu(111) substrates (Fig. 2) [14,30]. Unlike Er, Ho shows a divalent configuration ($4f^{11}$) on both crystallographic faces of Ag.

(c) Dysprosium (Dy): The trivalent ground state of Dy, i.e., $4f^9$ occupation [30] is observed only on Pt(111) (Fig. 3). The divalent configuration, i.e., $4f^{10}$ occupation is observed for adsorption on all the three other surfaces.

(d) Thulium (Tm): The absence of the M_4 peak in the Tm spectra obtained for adsorption on Cu(111) indicates its divalent state, which has only one hole in the $4f$ shell [30,52]. This is further confirmed by comparing the spectra with simulations obtained for the trivalent and divalent case (Fig. 4).

The $4f$ occupancy in RE atoms is determined by the following two quantities, (a) the energy needed to change from a divalent to a trivalent atomic ground state, which is represented by the sum of atomic correction energies, i.e., $4f \rightarrow 5d$ promotion energy E_{fd} + intershell coupling energy δE_c [21,36] and (b) the difference in binding energy between the trivalent [E_b(III)] and divalent state [E_b(II)] (Fig. 5). The former is essentially an atomic quantity, whereas the latter emerges from the hybridization of the valence electrons with the substrate bands. In the bulk of most RE elements, the presence of an additional electron in the spd-band allows the binding energy term to largely overcome $E_{fd} + \delta E_c$, hence the trivalent configuration becomes favorable [20,21]. On the other hand, in low coordinated systems such as clusters [19,36], surfaces [32–34] or single atoms at surfaces, E_b

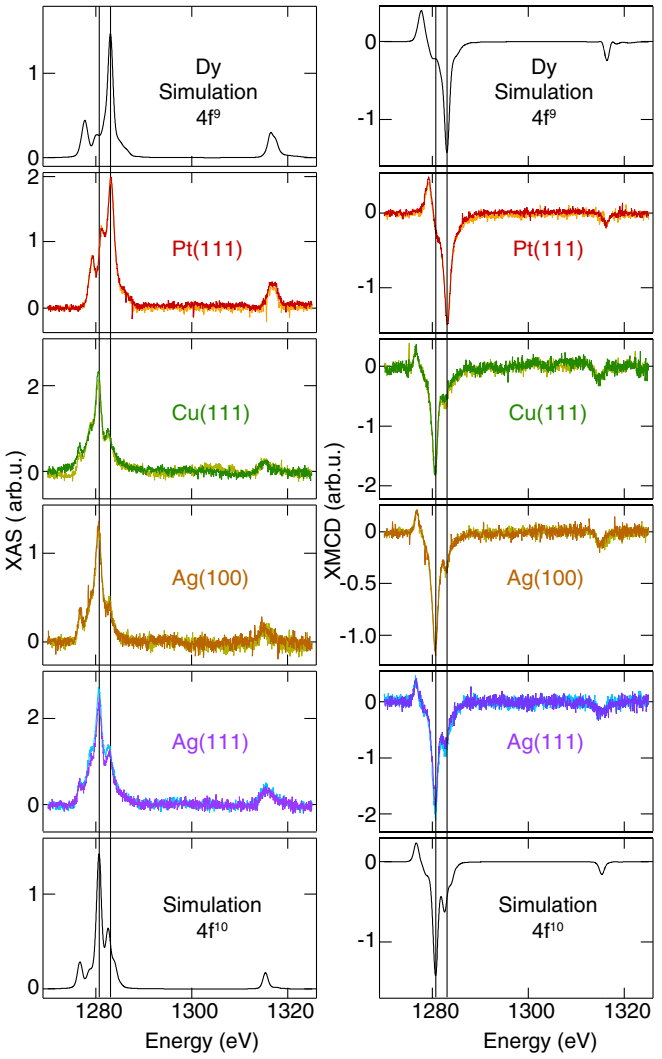

FIG. 3. XAS and XMCD of 0.004, 0.009, 0.003, and 0.006 ML Dy on Pt(111), Cu(111), Ag(100), and Ag(111), respectively. All spectra are measured at 6.8 T apart from the ones of Dy/Cu(111), and Dy/Ag(111), which are measured at 5 T. Normal (grazing) incidence spectra are shown in darker (lighter) color. Multiplet simulations of the trivalent and divalent state are shown in top and bottom panels.

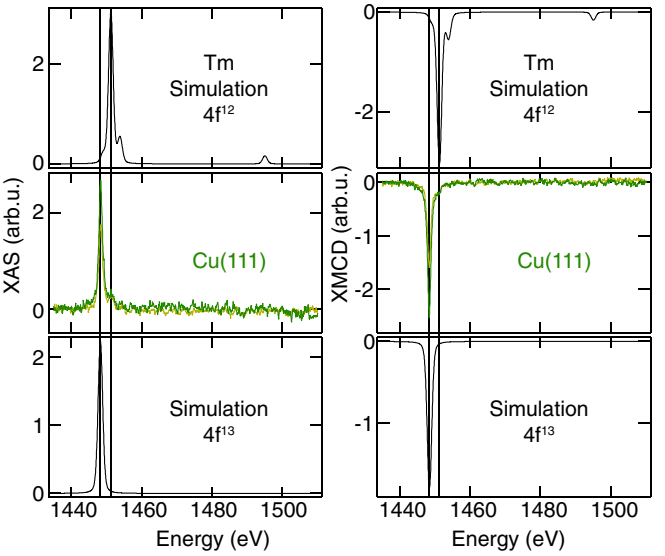

FIG. 4. XAS and XMCD of 0.010 ML Tm on Cu(111). Normal (grazing) incidence spectra are shown in darker (lighter) color. The top and bottom panels show multiplet simulations of the trivalent and divalent state.

becomes comparable to $E_{fd} + \delta E_c$ and both divalent and trivalent states have been observed [11,14,17,18].

Table II summarizes the values of $E_{fd} + \delta E_c$ [20,21,36], and the trends in the $4f$ occupation for surface adsorption. Here, the RE atoms are sorted by their value of $E_{fd} + \delta E_c$, while the substrates are sorted by the density of states (DOS) at the Fermi level E_F as reported in Ref. [53]. The trend in $E_{fd} + \delta E_c$ suggests that the stability of the trivalent state among the investigated elements is the lowest for Tm and the highest for Er [20,22,54]. In agreement with this description, Er is found mostly in the trivalent state while the occurrence of the divalent configuration increases with increasing $E_{fd} + \delta E_c$.

The importance of the binding term in the energy balance is reflected in the variation of the $4f$ occupation with the nature of the substrate. We find that Ho, Dy, and Er possess a $4f^{n-1}$ configuration on Pt(111) and a $4f^n$ configuration on Ag substrates [except for Er on Ag(100)]. This can be rationalized by looking at the connection between the substrate density of states (DOS) at E_F and the binding energy of an adsorbate. All the substrates considered in this work possess wide s and p bands, while the contribution of the narrower d bands to the DOS at E_F increases from Ag to Pt [53,55]. The hybridization between the outer $6s6p5d$ orbitals of the RE with the substrate conduction electrons produces hybrid RE-metal bands, the DOS of which at E_F is enhanced when substrate d bands are available [56]. A higher degree of hybridization leads to the stabilization of the trivalent state, which requires one of the $4f$ electrons to be promoted to these hybrid RE-metal bands. In good agreement with this picture, we observe that Pt(111) stabilizes the trivalent states in all the REs while Ag(111) induces the divalent state (Table II).

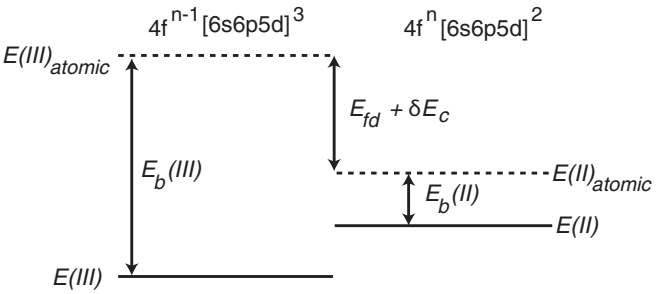

FIG. 5. Scheme of total atomic correction energy, namely, the sum of $4f \rightarrow 5d$ promotion energy E_{fd} and intershell coupling energy δE_c, and binding energies in di- and trivalent states, i.e., E_b(II) and E_b(III), respectively, influencing the $4f$ occupancy in rare earths. The ground-state energies for the free atoms in their di- and trivalent states are indicated as $E(\mathrm{II})_{\mathrm{atomic}}$ and $E(\mathrm{III})_{\mathrm{atomic}}$, respectively. The corresponding values for surface-supported atoms are E(II) and E(III).

TABLE II. $4f$ occupations of the REs on different metal substrates. Here the divalent and trivalent states are addressed as $4f^n$ and $4f^{n-1}$, respectively. The values of n are the same as in Table I. The sum $E_{fd}+\delta E_c$ is an atomic quantity which represents the energy cost to change from the divalent to the trivalent atomic ground state [21].

Rare earths	$E_{fd}+\delta E_c$ eV	Substrates			
		Pt(111)	Cu(111)	Ag(100)	Ag(111)
Er	1.16	$4f^{n-1}$	$4f^{n-1}$	$4f^{n-1}$	$4f^n$
Ho	1.30	$4f^{n-1}$	$4f^{n-1}$	$4f^n$	$4f^n$
Dy	1.45	$4f^{n-1}$	$4f^n$	$4f^n$	$4f^n$
Tm	2.06	–	$4f^n$	–	–

As the surface projected bulk DOS and thus the binding energy E_b depends on the surface coordination, the $4f$ occupation of Er also changes from $4f^{n-1}$ to $4f^n$ moving from Ag(100) to Ag(111) (Table II). E_b is expected to be larger on Ag(100) with respect to Ag(111) as the higher coordination of the RE atom on Ag(100) enforces a stronger binding. Consistent with this description, the RE with the highest $E_{fd}+\delta E_c$, i.e., Er, shows a trivalent state on Ag(100) and a divalent one on Ag(111). The different binding environment also produces different strength of CF as detailed in Sec. III C.

The correlation between increasing binding energy and stability of the trivalent state is further evident from the evolution of XAS and XMCD as a function of RE coverage for Dy and Er on Ag(111) (Figs. 6 and 7). These atoms are predominantly divalent as monomers, i.e., for coverages below 0.02 ML (Figs. 3 and 2), whereas the signature of the trivalent state becomes more pronounced with increasing coverage (Figs. 6 and 7). Larger coverages imply increased abundance of RE clusters formed by atoms landing within the direct capture zone of already present adatoms [16]. The increased coordination among the RE atoms enables the formation of

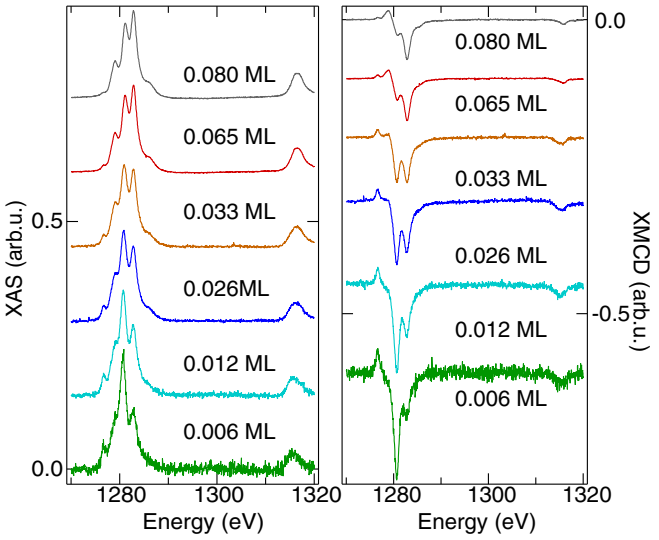

FIG. 6. Coverage dependent XAS and XMCD measurement at $\theta = 0^\circ$ of Dy on Ag(111). Hybridization with the surrounding RE atoms increases at larger Dy coverages and this stabilizes the trivalent state. Spectra are offset for clarity and normalized to the total XAS.

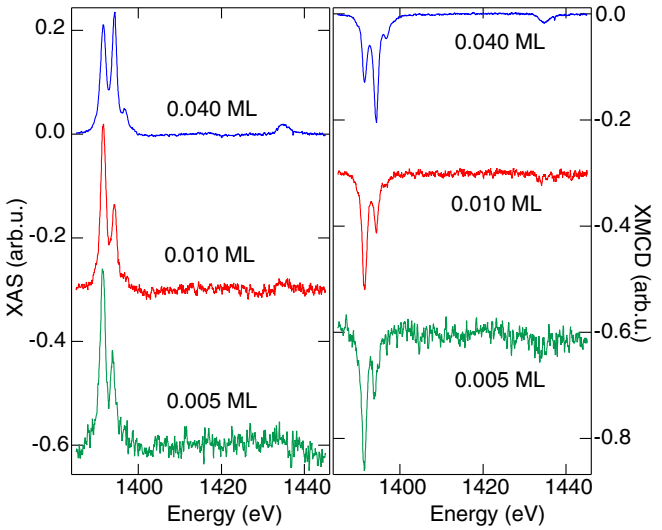

FIG. 7. Coverage-dependent XAS and XMCD studies at $\theta = 0^\circ$ of Er on Ag(111). The divalent state is observed up to 0.01 ML, while larger contribution from the trivalent state is observed at 0.04 ML. The spectra are offset for clarity and normalized to the total XAS.

RE-RE valence bands, which allows efficient transfer of one electron from the $4f$ to the $[6s6p5d]$ bands [19]. Note that for surface-adsorbed atoms which are already trivalent, the $4f$ occupancy does not change with increasing coordination at larger coverages, as it has been previously shown for Er on Cu(111) [16].

B. Magnetic moment and anisotropy

In order to extract the spin and orbital magnetic moments per atom from XAS and XMCD, we apply the sum rules. For the different RE-substrate combinations, the $\langle J_z \rangle$ values are presented in Table III for the two angles of incidence while their detailed sum rule analysis is shown in Appendix C (Tables VI and VII). Note that for Er/Ag(111) and Tm/Cu(111) we observe a strong angular dependence in total XAS [Figs. 1, 11(a), and 4]. Therefore the assumption of isotropic absorption does not hold for these cases [47] and additional theoretical knowledge is required to extract the true J_z, as will be shown in Sec. III C. For all other samples, the sum rule analysis suffices

TABLE III. $\langle J_z \rangle$ in units of $\hbar$ derived from sum rules for the REs on different metal substrates for the two angles of incidence.

Rare earths	θ	Substrates			
		Pt(111)	Cu(111)	Ag(100)	Ag(111)
Er	0°	5.6±0.1	1.0±0.1	6.1±0.1	3.9±0.2
	60°	3.7±0.1	5.0±0.2	5.7±0.1	3.5±0.1
Ho	0°	5.5±0.1	6.9±0.2	4.4±0.1	6.5±0.2
	60°	5.1±0.1	4.9±0.1	4.6±0.1	6.0±0.1
Dy	0°	6.8±0.2	6.3±0.2	6.3±0.2	6.0±0.1
	60°	6.8±0.2	5.9±0.2	6.4±0.2	6.4±0.2
Tm	0°	–	2.2±0.2	–	–
	60°	–	1.9±0.1	–	–

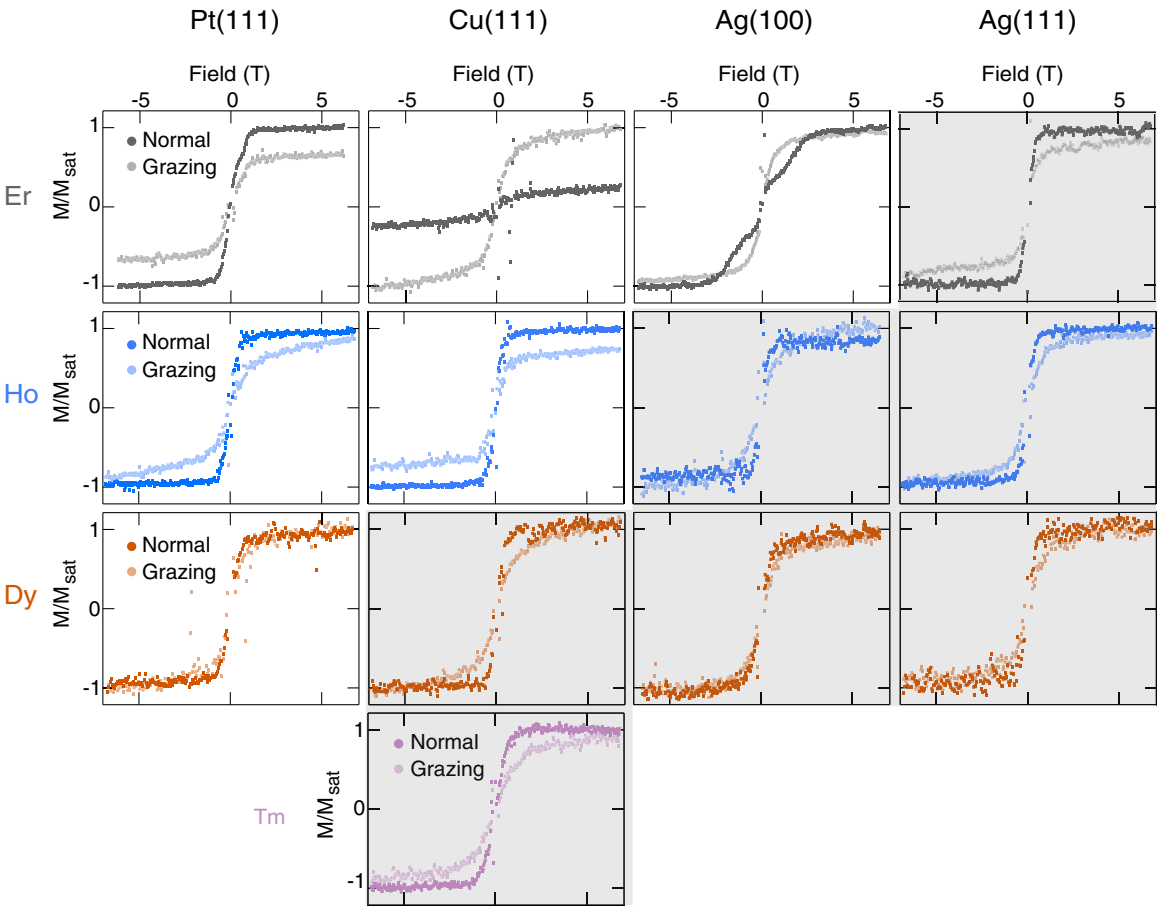

FIG. 8. Magnetization curves measured for different adatom-substrate combinations. RE coverages are the same as mentioned earlier in Figs. 1–4 for the respective samples. Similar to Table II the magnetization curves shaded in grey are from REs in $4f^n$ configuration, while the rest are for REs in $4f^{n-1}$ configuration.

because the deviation from the isotropic absorption is at least three times smaller than those observed in Er/Ag(111) and Tm/Cu(111) (Table IX).

In order to determine the orientation of the magnetic easy axis, we measure the angular dependence of the magnetization curves $M(\mu_0 H)$ (Fig. 8) and we follow the trend of $R = \frac{\langle M_{\rm tot}\rangle @ 0^\circ}{\langle M_{\rm tot}\rangle @ 60^\circ}$ (where all $\langle M_{\rm tot}\rangle$ values are calculated at 6.8 T using only sum rules) (Fig. 9). The $M(\mu_0 H)$ curves illustrate the field dependence of the total magnetic moment of the atom under investigation. Therefore the angular contrast observed in $M(\mu_0 H)$ contains information about the magnetic anisotropy of the system. On the other hand, R is a quantity that can be related to the MAE and easily calculated from the sum rule values obtained previously. Note that, both $M(\mu_0 H)$ curves and R only qualitatively represent the anisotropy of the XAS and XMCD in the following discussion. They can be connected to the classical magnetic anisotropy only if the ground state has maximum or minimum $\langle J_z\rangle$ and the anisotropy barrier is monotonic. In this qualitative representation, $R \approx 1$ indicate very low MAE, while $R > 1$ and $R < 1$ correspond to out-of-plane easy and hard axis, respectively.

From Figs. 8 and 9, one can immediately discern that for a substrate with a given coordination number, divalent RE atoms exhibit less anisotropy than the trivalent ones. This can be attributed to the larger covalent radius corresponding to a larger bonding distance in the divalent case [57], which reduces the overlap with the substrate's d bands and results in a less anisotropic ligand environment. The bonding environment also dictates the anisotropy of an atom of the same valency on

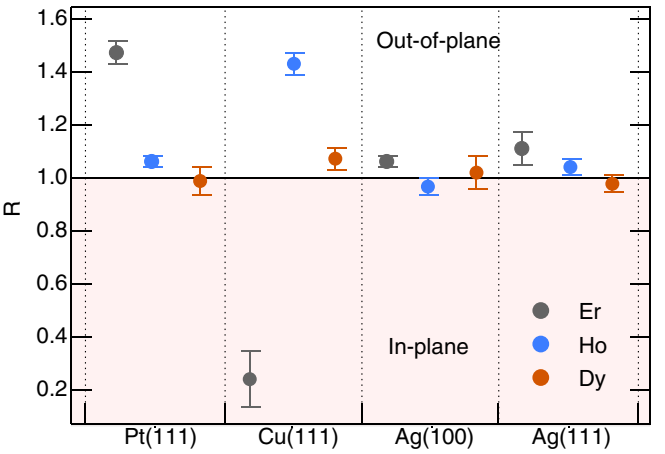

FIG. 9. $R = \frac{\langle M_{\rm tot}\rangle @ 0^\circ}{\langle M_{\rm tot}\rangle @ 60^\circ}$ for different adatom-substrate combination. The shaded region indicates preferred in-plane magnetization.

different (111) substrates. Figure 9 illustrates that for such cases, R values are larger for adsorption on Pt(111) and Cu(111) compared to Ag. We ascribe this to the increasing degree of overlap between the RE spd states and the d bands from the substrates along the Ag→Cu→Pt series, as described in Sec. III A. Note that no hysteresis opening has been observed in any of these magnetization curves i.e., the lifetime of the magnetic states is shorter than about ten seconds. We ascribe this lack of magnetic stability to the interaction with the conduction electrons and the soft phonon modes of the metal substrate, as mentioned in previous works [14,18].

C. Crystal field and 4f occupancy: Er atoms on Ag(100) and Ag(111)

In order to gain insight into the interplay between surface binding, 4f occupation, and strength of the CF, we employed multiplet analysis which models the effective CF generated by the ligand charges at the surface as point charges (Table V). This approach allows us to determine the quantum level structures of Er atoms exposed to different CF environments. The CF potential, which is given by the position and strength of such point charges, is a measure of RE-substrate interaction. In particular, this approach is best suited for the 4f states as their highly localized character reduces the interaction of the REs with the surrounding atoms to a purely electrostatic nature [14,58–60]. Moreover, Er is the ideal prototype for this analysis since it exhibits different occupancies on the two crystallographic faces of Ag and this further allows us to gain insight into the effects of CF and coordination.

We start with the case of Er on Ag(100). This system exhibits a change of the slope in the normal incidence $M(\mu_0 H)$ curves at around 1.2 T. This feature hints to a switch of the magnetic state from low to high J_z triggered by the Zeeman energy. Such field-induced crossovers of magnetic states have been reported in molecular magnets [61,62] and Fe atoms on Pt(111) [63]. This peculiar shape of the magnetization curves, as well as the XAS spectra acquired at different fields, allow us to determine the magnetic level splitting with very high accuracy.

The results of simultaneous fitting of all experimental XAS and XMCD spectra are presented in Figs. 10(a)–10(c). Application of sum rules to the spectra simulated for 6.8 T yields comparable total magnetic moments $\langle M_{\rm tot}\rangle = 2\langle S_z\rangle + 6\langle T_z\rangle + \langle L_z\rangle$ (Table IV). Magnetization curves are simulated by calculating the maximum XMCD at the M_5 edge as a function of $\mu_0 H$ [Fig. 10(d)]. The simulated curve at $\theta = 0^\circ$ reproduces well the change of slope at around 1.2 T and the grazing curve is also very well matched. Additional confirmation of our model comes from the excellent agreement between experimental and calculated field dependent XAS spectra, see Fig. 10(c). As expected for a paramagnetic system, the corresponding XMCD also show a monotonic increase of the central peak at 1394.3 eV (data not shown). The simulated curve for 0° deviates from the experimental one for $\mu_0 H < 1.5$ T, in particular it does not exhibit the sharp step at 0.2 T. The maximum deviation is about 25% of the saturation. We ascribe this deviation to the presence of small clusters (e.g., dimers), the amount of which can be about 10% at this coverage [18,64]. This can contribute 20% of the total absorption signal (assuming all of them as dimers). The magnetization curve of such clusters is likely to show a steeper slope at small fields owing to their larger moments. Note that the magnetic properties of surface-supported RE atoms (e.g., magnetic moment and easy axis) can differ from the small clusters as reported in Ref. [16]. Since both atoms and clusters are trivalent on this surface, their XMCD signatures appear at the same energy and the overall signal is a superposition of the two relative contributions (Fig. 1).

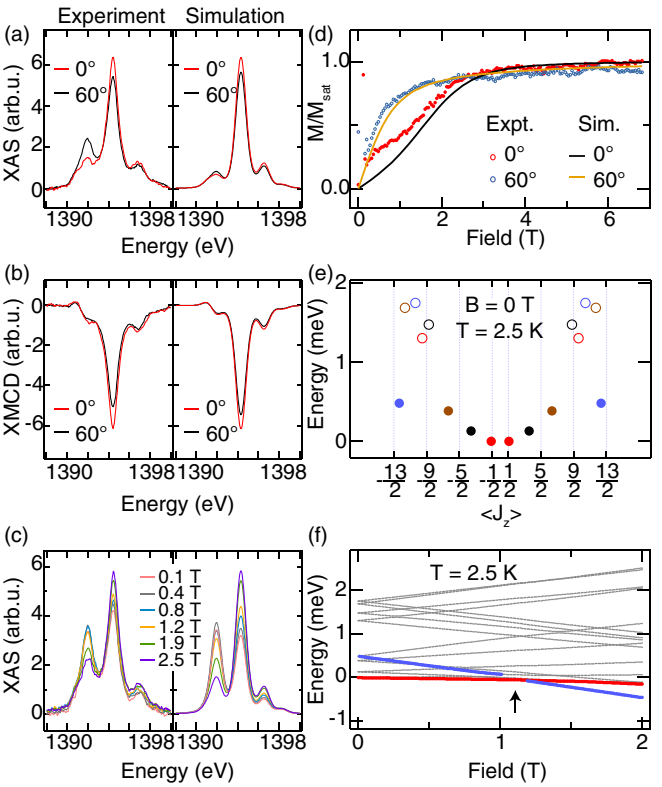

FIG. 10. Er/Ag(100): Comparison between experimental and simulated (a) XAS, (b) XMCD at $\mu_0 H = 6.8$ T, (c) XAS for different $\mu_0 H$ at $\theta = 0^\circ$, and (d) magnetization curves. (e) Energy splitting of the ground-state multiplet calculated for $\mu_0 H = 0$ T and (f) Zeeman diagram for the same levels. The arrow indicates the sharp change in the magnetic moment at $\mu_0 H = 1.16$ T, due to the crossing between the $\langle J_z\rangle \approx \pm 1/2$ (in red) and the $\langle J_z\rangle \approx= \pm 13/2$ states (in blue). $T = 2.5$ K, Er coverage = 0.014 ML.

The corresponding level distribution of the ground state multiplet for $\mu_0 H = 0$ T indicates a ground state with $\langle J_z\rangle = \pm 0.6$ [Fig. 10(e)]. The overall energy splitting is about

TABLE IV. Comparison between experimental and simulated out-of-plane projected magnetic moments at $\mu_0 H = 6.8$ T for Er atoms adsorbed on Ag(100) and Ag(111). The $\langle M_{\rm tot}\rangle$ values are obtained from sum rules applied on the experimental and simulated spectra.

Substrate	$\langle M_{\rm tot}\rangle(\mu_B)$ Expt.(Table VI)	Sim.	$\langle J_z\rangle(\hbar)$ Expt. (Table III)	Sim.
Ag(100)	8.8±0.1	9.8	6.1±0.1	7.4
Ag(111)	5.7±0.3	5.7	3.9±0.2	6.0

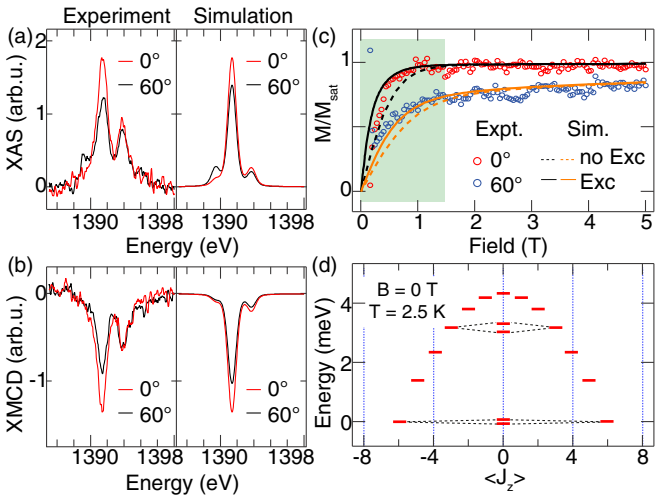

FIG. 11. Er/Ag(111). Comparison between experimental and simulated (a) XAS, (b) XMCD (Er coverage 0.005 ML), and (c) magnetization curves (Er coverage 0.01 ML). The region of the $M(\mu_0 H)$ curves shaded in green highlights the impact of ferromagnetic exchange coupling among the Er atoms. (d) Energy splitting of the magnetic quantum levels. The splitting of the ± 6 states has been blown up by a factor of 60 for clarity.

one order of magnitude smaller than those reported for Er adsorbed on Pt(111) and Cu(111) [14]. In particular, the proximity of excited states with larger $\langle J_z \rangle$ suggests the potential level crossing in the presence of a finite magnetic field. The field dependence of the magnetic quantum levels sketched in Fig. 10(f) indicates that this level crossing occurs at $\mu_0 H = 1.16$ T as marked by the black arrow. Consequently, the ground state $\langle J_z \rangle$ changes from ± 0.6 at 0 T to ± 7.4 at 6.8 T (Table IV). Note that the simulated ground state of $\langle J_z \rangle = \pm 7.4$ (Table IV) at 6.8 T is different than the maximum $\langle J_z \rangle \approx \frac{13}{2}$ presented in Fig. 10(e) for $\mu_0 H = 0$ T. At zero field, the magnetic levels are mixed and therefore none of them correspond to the ideal half-integer value of J_z. The finite magnetic field breaks this mixing and we observe the almost maximum value achievable within the $J = 15/2$ multiplet of Er in $4f^{11}$ configuration.

Similarly, multiplet calculations were done for Er atoms adsorbed on Ag(111) by comparing simulations and experiments as shown in Figs. 11(a) and 11(b). The excellent match between the values of $\langle M_{\text{tot}} \rangle$, obtained by applying the sum rules on both simulated and experimental spectra at 6.8 T, confirms the accuracy of our simulations (Table IV). The resulting ground state at the maximum field has $\langle J_z \rangle = 6.0$ (Table IV), corresponding to the maximum value of $\langle J_z \rangle$ for the $4f^{12}$ configuration. The threefold symmetry of Ag(111) quenches the $\langle J_z \rangle = \pm 6$ and ± 3 states [indicated as black dotted lines in Fig. 11(d)]. This results in two pairs of mixed states with $\langle J_z \rangle = 0$ which are split by 2.2 μeV and 0.3 meV respectively. We note that the calculated value of $\langle J_z \rangle$ at 6.8 T, which is directly obtained as the output of the simulation, significantly differs from that derived using the experimental sum rules (Table III). This discrepancy stems from the application of the sum rules to systems with pronounced angular anisotropy in the corresponding XAS, for which the isotropic assumption on the XAS integral does not hold [65]. Hence, for such cases, the sum rule analysis is not accurate enough for drawing meaningful conclusions on the magnetic ground state, rather a detailed multiplet analysis is strictly required.

A zoom into the magnetization curves of this system is shown in Fig. 11(c). Similar to the case of Er/Ag(100), the simulated $M(\mu_0 H)$ curves perfectly match with the measured saturated magnetization at the highest applied field. However, the slope of $M(\mu_0 H)$ in low fields are not reproduced at both normal and grazing incidence. The presence of statistically grown clusters cannot account for this discrepancy because, differently from the measurements on Ag(100), the signal coming from atoms and clusters can be easily identified, thanks to their two characteristic energies in the XMCD (Fig. 7). In particular, the clusters contribute to the signal at 1394.3 eV that corresponds to the trivalent peak while the $M(\mu_0 H)$ curves are acquired at 1391.4 eV corresponding to the divalent peak (Fig. 7).

Therefore we attribute the discrepancy to the presence of ferromagnetic exchange among the Er atoms. In Appendix A, we argue that the agreement can be improved by introducing ferromagnetic exchange with a Curie temperature of 0.55 K. The corresponding best fit is shown as solid lines in Fig. 11(c).

Finally, to pinpoint the effect of the different CFs on the magnetic states of Er adatoms, we compare the strength of the CF potential generated by the two substrates. Within the point charge approximation, this is defined as $V(r) = \sum_{m=1}^{N_{\text{ions}}} (Q_m/|r - R_m|)$ [48], where N_{ions} is the total number of point charges Q_m at position R_m from the atom of interest. Using the values presented in Table V, we obtain $|V(r)| = 0.55\, e/\text{Å}$ and $0.02\, e/\text{Å}$ for Ag(100) and Ag(111), respectively, confirming a significantly stronger CF on Ag(100). Note that despite this stronger CF, the total level splitting on Ag(100) remains lower as the fourfold symmetric charge distribution makes the CF less uniaxial compared to the case of Ag(111). Interestingly, the higher coordination offered by the Ag(100) surface is both responsible for stabilizing the trivalent state and inducing a stronger CF. These effects follow from the larger E_b inferred for this surface compared to Ag(111), which ultimately leads to a stronger RE-metal hybridization and a significantly different charge distribution (Table V).

IV. CONCLUSION

Combining XAS and XMCD measurements with multiplet analysis, we have shown that RE single atoms can possess both trivalent and divalent states when adsorbed on metal substrates. We have demonstrated that the trivalent state is achieved in presence of (a) low $E_{fd} + \delta E_c$ of the RE under investigation and (b) strong binding with the surrounding environment. Under such constraints, Er shows the highest propensity towards the trivalent state whereas we expect Tm to have the divalent configuration. Among the substrates, Pt(111) provides the highest degree of hybridization owing to the largest DOS at E_F. Finally, the angular dependence of the total magnetic moment and magnetization curves evidence that, for the same substrate and coordination number, RE atoms that are divalent exhibit less anisotropy than the trivalent ones. On the other hand, for the REs of a given valency, we ascribe

the difference in anisotropy to the degree of overlap with the surface d bands.

ACKNOWLEDGMENTS

We acknowledge funding from the Swiss National Science Foundation (SNSF) through Grants 200020_157081/1 (A.S.), 200021_146715/1 (R.B.), and PZ00P2_142474 (C.W. and J.D.). L.P. was supported by an ETH Postdoctoral Fellowship (FEL-42 13-2). We thank A. Uldry and B. Delley for providing us with the updated version of the MULTIX software. M. Pivetta and K. Diller are acknowledged for fruitful discussions.

APPENDIX A: FERROMAGNETIC EXCHANGE: Er/Ag(111)

For atoms adsorbed on a metallic surface, substrate mediated interactions such as the Ruderman-Kittel-Kasuya-Yosida (RKKY) are activated [66,67]. The RKKY exchange is spatially modulated as $J_0 \frac{\cos(2rk_F)}{(2rk_F)^2}$, where J_0 represents the interaction strength, r is the distance among the atoms within the superlattice, and k_F is the Fermi wave vector [68–70]. Thus, for distributions of statistically adsorbed single atoms, the effect is usually negligible due to the random arrangements and large distances among the atoms. For atoms deposited on Ag(111) the situation is different. The surface state electrons of Ag(111) promote a regular arrangement of the Er atoms thus ordering them in a superlattice [16,68,71]. The superlattice introduces coherent interactions among atoms thus leading to a magnetic ordering of the Er atoms on Ag(111). Therefore we recalculate the $M(\mu_0 H)$ curves including such exchange interaction. Given the low magnetic anisotropy of the system, we consider Heisenberg coupling among the spins as it has been shown by Umbach *et al.* [70]. Within the mean-field description, the effective magnetic field can be written as $H_{\text{eff}} = \mu_0 H + H_{\text{exc}} = \mu_0 H + \kappa \times g \langle J_z(H_{\text{eff}}) \rangle \mu_B = \mu_0 H + \kappa \times M(H_{\text{eff}})$, where κ is an empirical constant, $\langle J_z(\mu_0 H) \rangle = 6.0\ \hbar$ in saturation as obtained from simulation, and $g = 7/6$ in the $4f^{12}$ configuration. As $M(H_{\text{eff}})$ is an implicit function of H_{eff}, we need to iteratively solve for $M(H_{\text{eff}})$, until we find the best agreement with the experimental data. The iteration starts with the $M(\mu_0 H)$ curves obtained from MULTIX simulations [dotted curves in Fig. 11(c)] and subsequently continues with the iterative calculations of H_{eff} in each step, until the solution converges, i.e., the difference between H^n_{eff} and H^{n+1}_{eff} is less than a set tolerance limit. The best fit provides $H_{\text{exc}} = 0.35$ T in saturation [Fig. 11(c)]. This further allows us to calculate the total exchange energy $J_{\text{exc}} = H_{\text{exc}} \times g \langle J_z(\mu_0 H) \rangle = 0.142$ meV. Considering that each Er atom has six neighbors, the onsite pair exchange energy reduces to $J_i = J_{\text{exc}}/6 = 0.024$ meV. This exchange interaction corresponds to a Curie temperature of $\sum_{i=1}^{6} J_i / 3k_B = 0.55$ K [70]. From the similarly steep $M(\mu_0 H)$ curves measured for both Ho and Dy on Ag(111), one can also speculate the presence of the same effect on those systems (Fig. 8).

In contrast, the magnetization curves of Ho and Er atoms on Cu(111) were reproduced using multiplet calculations without the need of any ferromagnetic exchange [14,16]. This indicates that the strength of such interaction, if any, is well below the measurement temperature for these elements on Cu(111). Since an ordered superlattice with period $r = \pi/k_F$ forms also on this surface, the absence of ferromagnetic exchange on Cu(111) hints towards the fact that J_0 of Ag(111) is larger than the one of Cu(111). Evaluation of J_0 is not very straightforward and it involves complex calculations [66]. Therefore within the scope of this work, we can only attribute the difference in the RKKY strength to the type of adatom-substrate interaction, which eventually leads to different fillings of the $4f$ orbitals.

APPENDIX B: MULTIPLET ANALYSIS

TABLE V. Crystal field used for the multiplet simulations of Er atoms on Ag(100) and Ag(111), respectively.

Substrates	x Å	y Å	z Å	Charge e
Ag(100)	2.04	2.04	−2.40	−0.6
	−2.04	2.04	−2.40	−0.6
	2.04	−2.04	−2.40	−0.6
	−2.04	−2.04	−2.40	−0.6
	0.0	0.0	−4.48	0.375
Ag(111)	1.669	0.0	−0.61	−0.0115
	−0.834	1.445	−0.61	−0.0115
	−0.834	−1.445	−0.61	−0.0115

APPENDIX C: SUM RULE ANALYSIS

TABLE VI. The expectation values of effective spin $\langle S_{\text{eff}} \rangle = 2\langle S_z \rangle + 6\langle T_z \rangle$, spin $\langle S_z \rangle$, orbital $\langle L_z \rangle$, and total $\langle J_z \rangle$ magnetic moments are expressed in units of $\hbar$, $\theta = 0^\circ$.

Rare earth	Substrate	Moments in $\hbar$			
		$\langle S_{\text{eff}} \rangle$	$\langle S_z \rangle$	$\langle L_z \rangle$	$\langle J_z \rangle$
Er	Pt(111)	3.5 ± 0.2	1.1 ± 0.1	4.5 ± 0.1	5.6 ± 0.1
	Cu(111)	1.0 ± 0.1	0.3 ± 0.0	0.7 ± 0.1	1.0 ± 0.1
	Ag(100)	3.8 ± 0.1	1.2 ± 0.0	4.9 ± 0.1	6.1 ± 0.1
	Ag(111)	2.4 ± 0.2	0.5 ± 0.1	3.3 ± 0.2	3.9 ± 0.2
Ho	Pt(111)	2.8 ± 0.1	1.3 ± 0.1	4.3 ± 0.1	5.5 ± 0.1
	Cu(111)	3.8 ± 0.2	1.7 ± 0.1	5.3 ± 0.2	6.9 ± 0.2
	Ag(100)	2.8 ± 0.1	0.9 ± 0.0	3.6 ± 0.1	4.4 ± 0.1
	Ag(111)	3.9 ± 0.2	1.2 ± 0.1	5.2 ± 0.1	6.5 ± 0.2
Dy	Pt(111)	4.1 ± 0.2	2.7 ± 0.1	4.1 ± 0.2	6.8 ± 0.2
	Cu(111)	3.8 ± 0.2	1.6 ± 0.1	4.7 ± 0.2	6.3 ± 0.2
	Ag(100)	3.7 ± 0.4	1.6 ± 0.2	4.8 ± 0.2	6.3 ± 0.2
	Ag(111)	4.2 ± 0.1	1.8 ± 0.1	4.3 ± 0.1	6.0 ± 0.1
Tm	Cu(111)	1.9 ± 0.0	0.3 ± 0.0	1.9 ± 0.0	2.2 ± 0.0

TABLE VII. The same as in Table VI for $\theta = 60^\circ$.

Rare earth	Substrate	Moments in $\hbar$			
		$\langle S_{\text{eff}} \rangle$	$\langle S_z \rangle$	$\langle L_z \rangle$	$\langle J_z \rangle$
Er	Pt(111)	2.5 ± 0.2	0.8 ± 0.1	2.9 ± 0.1	3.7 ± 0.1
	Cu(111)	3.2 ± 0.1	1.0 ± 0.1	4.0 ± 0.2	5.0 ± 0.2
	Ag(100)	3.7 ± 0.1	1.1 ± 0.1	4.6 ± 0.1	5.7 ± 0.1
	Ag(111)	2.7 ± 0.1	0.6 ± 0.1	2.4 ± 0.1	3.0 ± 0.1
Ho	Pt(111)	2.9 ± 0.1	1.3 ± 0.0	3.8 ± 0.1	5.1 ± 0.1
	Cu(111)	2.6 ± 0.2	1.1 ± 0.1	3.8 ± 0.1	4.9 ± 0.1
	Ag(100)	2.8 ± 0.1	0.8 ± 0.0	3.7 ± 0.1	4.6 ± 0.1
	Ag(111)	4.0 ± 0.1	1.2 ± 0.0	4.8 ± 0.1	6.1 ± 0.1
Dy	Pt(111)	4.1 ± 0.2	2.7 ± 0.1	4.1 ± 0.2	6.8 ± 0.2
	Cu(111)	3.6 ± 0.1	1.5 ± 0.0	4.4 ± 0.2	5.9 ± 0.2
	Ag(100)	3.2 ± 0.2	1.4 ± 0.1	5.0 ± 0.2	6.4 ± 0.2
	Ag(111)	4.0 ± 0.1	1.7 ± 0.1	4.7 ± 0.2	6.4 ± 0.2
Tm	Cu(111)	1.7 ± 0.1	0.3 ± 0.0	1.7 ± 0.1	2.0 ± 0.0

APPENDIX D: $\langle T_z \rangle$ CALCULATION

TABLE VIII. Comparison of $\langle T_z \rangle$ values for the trivalent RE ions.

Reference	$\langle T_z \rangle$ in units of ($\hbar$)			
	Dy	Ho	Er	Tm
Ref. [39], Eq. (8) (free ions)	−0.333	−0.133	+0.133	+0.333
Present work	+0.186	−0.086	−0.301	−0.392
Ref. [49], Table I	+0.128	−0.137	−0.313	−0.407

APPENDIX E: TIME EVOLUTION OF ABSORPTION SPECTRA

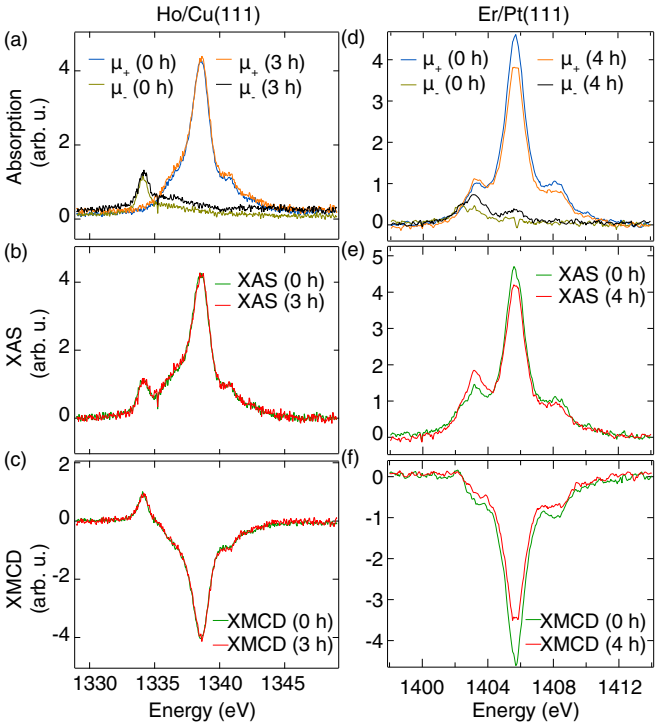

FIG. 12. Time evolution of the absorption signals at 6.8 T, from the two circular polarizations μ_+ and μ_- in (a) and (d), XAS in (b) and (e), and XMCD in (c) and (f) for 0.009 and 0.012 ML of Ho on Cu(111) and Er on Pt(111), respectively. (a)–(c) indicate no significant changes in the peak heights after 3 hours from the deposition of the RE. However, for Er/Pt(111), such effects are significant 4 hours after the deposition (d)–(f).

APPENDIX F: ANISOTROPY IN TOTAL INTEGRATED XAS

TABLE IX. The ratio $\text{XAS}_{0^\circ}/\text{XAS}_{60^\circ}$ is derived by integrating the area under the XAS spectra within the $M_{4,5}$ region for the two angles of incidence for each adatom-substrate combination.

Rare earths	$\text{XAS}_{0^\circ}/\text{XAS}_{60^\circ}$			
	Pt(111)	Cu(111)	Ag(100)	Ag(111)
Er	1.05	0.97	1.06	**1.19**
Ho	0.97	1.03	1.02	1.04
Dy	0.97	1.08	0.96	0.95
Tm	–	**1.18**	–	–

[1] P. Gambardella, S. Rusponi, M. Veronese, S. S. Dhesi, C. Grazioli, A. Dallmeyer, I. Cabria, R. Zeller, P. H. Dederichs, K. Kern, C. Carbone, and H. Brune, Science **300**, 1130 (2003).

[2] H. Brune and P. Gambardella, Surf. Sci. **603**, 1812 (2009).

[3] P. Błoński, A. Lehnert, S. Dennler, S. Rusponi, M. Etzkorn, G. Moulas, P. Bencok, P. Gambardella, H. Brune, and J. Hafner, Phys. Rev. B **81**, 104426 (2010).

[4] C. Carbone, M. Veronese, P. Moras, S. Gardonio, C. Grazioli, P. H. Zhou, O. Rader, A. Varykhalov, C. Krull, T. Balashov, A. Mugarza, P. Gambardella, S. Lebègue, O. Eriksson, M. I. Katsnelson, and A. I. Lichtenstein, Phys. Rev. Lett. **104**, 117601 (2010).

[5] P. Gambardella, A. Dallmeyer, K. Maiti, M. C. Malagoli, W. Eberhardt, K. Kern, and C. Carbone, Nature (London) **416**, 301 (2002).

[6] C. F. Hirjibehedin, C.-Y. Lin, A. F. Otte, M. Ternes, C. P. Lutz, B. A. Jones, and A. J. Heinrich, Science **317**, 1199 (2007).

[7] A. Lehnert, S. Rusponi, M. Etzkorn, S. Ouazi, P. Thakur, and H. Brune, Phys. Rev. B **81**, 104430 (2010).

[8] I. G. Rau, S. Baumann, S. Rusponi, F. Donati, S. Stepanow, L. Gragnaniello, J. Dreiser, C. Piamonteze, F. Nolting, S. Gangopadhyay, O. R. Albertini, R. M. Macfarlane, C. P. Lutz, B. A. Jones, P. Gambardella, A. J. Heinrich, and H. Brune, Science **344**, 988 (2014).

[9] F. Donati, L. Gragnaniello, A. Cavallin, F. D. Natterer, Q. Dubout, M. Pivetta, F. Patthey, J. Dreiser, C. Piamonteze, S. Rusponi, and H. Brune, Phys. Rev. Lett. **113**, 177201 (2014).

[10] G. E. Pacchioni, L. Gragnaniello, F. Donati, M. Pivetta, G. Autès, O. V. Yazyev, S. Rusponi, and H. Brune, Phys. Rev. B **91**, 235426 (2015).

[11] C. Nistor, A. Mugarza, S. Stepanow, P. Gambardella, K. Kummer, J. L. Diez-Ferrer, D. Coffey, C. de la Fuente, M. Ciria, and J. I. Arnaudas, Phys. Rev. B **90**, 064423 (2014).

[12] T. Schuh, T. Miyamachi, S. Gerstl, M. Geilhufe, M. Hoffmann, S. Ostanin, W. Hergert, A. Ernst, and W. Wulfhekel, Nano Lett. **12**, 4805 (2012).

[13] T. Miyamachi, T. Schuh, T. Markl, C. Bresch, T. Balashov, A. Stohr, C. Karlewski, S. Andre, M. Marthaler, M. Hoffmann, M. Geilhufe, S. Ostanin, W. Hergert, I. Mertig, G. Schon, A. Ernst, and W. Wulfhekel, Nature (London) **503**, 242 (2013).

[14] F. Donati, A. Singha, S. Stepanow, C. Wäckerlin, J. Dreiser, P. Gambardella, S. Rusponi, and H. Brune, Phys. Rev. Lett. **113**, 237201 (2014).

[15] M. Steinbrecher, A. Sonntag, M. dos Santos Dias, M. Bouhassoune, S. Lounis, J. Wiebe, R. Wiesendanger, and A. A. Khajetoorians, Nat. Commun. **7**, 10454 (2015).

[16] A. Singha, F. Donati, C. Wäckerlin, R. Baltic, J. Dreiser, M. Pivetta, S. Rusponi, and H. Brune, Nano Lett. **16**, 3475 (2016).

[17] F. Donati, S. Rusponi, S. Stepanow, C. Wäckerlin, A. Singha, L. Persichetti, R. Baltic, K. Diller, F. Patthey, E. Fernandes, J. Dreiser, Ž. Šljivančanin, K. Kummer, C. Nistor, P. Gambardella, and H. Brune, Science **352**, 318 (2016).

[18] R. Baltic, M. Pivetta, F. Donati, C. Wäckerlin, A. Singha, J. Dreiser, S. Rusponi, and H. Brune, Nano Lett. **16**, 7610 (2016).

[19] L. Peters, S. Ghosh, B. Sanyal, C. van Dijk, J. Bowlan, W. de Heer, A. Delin, I. di Marco, O. Eriksson, M. I. Katsnelson, B. Johansson, and A. Kirilyuk, Sci. Rep. **6**, 19676 (2016).

[20] B. Johansson, Phys. Rev. B **20**, 1315 (1979).

[21] A. Delin, L. Fast, B. Johansson, J. M. Wills, and O. Eriksson, Phys. Rev. Lett. **79**, 4637 (1997).

[22] G. Meyer, Chem. Rev. **88**, 93 (1988).

[23] A. Kotani and Y. Toyozawa, J. Phys. Soc. Jpn. **35**, 1073 (1973).

[24] O. Gunnarsson and K. Schönhammer, Phys. Rev. Lett. **50**, 604 (1983).

[25] J. C. Parlebas and A. Kotani, J. Appl. Phys. **57**, 3191 (1985).

[26] Y. Hammoud, J. C. Parlebas, and F. Gautier, J. Phys. C: Solid State Phys. **18**, 6603 (1985).

[27] T. Jo, Prog. Theor. Phys. Suppl. **101**, 303 (1990).

[28] N. Mårtensson, B. Reihl, R. A. Pollak, F. Holtzberg, G. Kaindl, and D. E. Eastman, Phys. Rev. B **26**, 648 (1982).

[29] J. B. Goedkoop, B. T. Thole, G. van der Laan, G. A. Sawatzky, F. M. F. de Groot, and J. C. Fuggle, Phys. Rev. B **37**, 2086 (1988).

[30] B. T. Thole, G. van der Laan, J. C. Fuggle, G. A. Sawatzky, R. C. Karnatak, and J.-M. Esteva, Phys. Rev. B **32**, 5107 (1985).

[31] E. Lundgren, J. N. Andersen, R. Nyholm, X. Torrelles, J. Rius, A. Delin, A. Grechnev, O. Eriksson, C. Konvicka, M. Schmid, and P. Varga, Phys. Rev. Lett. **88**, 136102 (2002).

[32] B. Johansson, Phys. Rev. B **19**, 6615 (1979).

[33] A. Stenborg, O. Björneholm, A. Nilsson, N. Mårtensson, J. N. Andersen, and C. Wigren, Phys. Rev. B **40**, 5916 (1989).

[34] G. K. Wertheim and G. Crecelius, Phys. Rev. Lett. **40**, 813 (1978).

[35] M. Domke, C. Laubschat, M. Prietsch, T. Mandel, G. Kaindl, and W. D. Schneider, Phys. Rev. Lett. **56**, 1287 (1986).

[36] L. Peters, I. Di Marco, M. S. Litsarev, A. Delin, M. I. Katsnelson, A. Kirilyuk, B. Johansson, B. Sanyal, and O. Eriksson, Phys. Rev. B **92**, 035143 (2015).

[37] P. Gambardella, S. S. Dhesi, S. Gardonio, C. Grazioli, P. Ohresser, and C. Carbone, Phys. Rev. Lett. **88**, 047202 (2002).

[38] B. T. Thole, P. Carra, F. Sette, and G. van der Laan, Phys. Rev. Lett. **68**, 1943 (1992).

[39] P. Carra, B. T. Thole, M. Altarelli, and X. Wang, Phys. Rev. Lett. **70**, 694 (1993).

[40] N. Ishikawa, M. Sugita, and W. Wernsdorfer, Angew. Chem., Int. Ed. **44**, 2931 (2005).

[41] R. Westerström, A.-C. Uldry, R. Stania, J. Dreiser, C. Piamonteze, M. Muntwiler, F. Matsui, S. Rusponi, H. Brune, S. Yang, A. Popov, B. Büchner, B. Delley, and T. Greber, Phys. Rev. Lett. **114**, 087201 (2015).

[42] C. Wäckerlin, F. Donati, A. Singha, R. Baltic, S. Rusponi, K. Diller, F. Patthey, M. Pivetta, Y. Lan, S. Klyatskaya, M. Ruben, H. Brune, and J. Dreiser, Adv. Mater. **28**, 5195 (2016).

[43] S. G. McAdams, A.-M. Ariciu, A. K. Kostopoulos, J. P. Walsh, and F. Tuna, Coord. Chem. Rev. **346**, 216 (2017).

[44] A. Abragam and B. Bleaney, *Electron Paramagnetic Resonance of Transition Ions* (Oxford University Press, Oxford, 1970).

[45] A. Singha, PhD thesis, EPFL, Switzerland, 2017.

[46] C. Piamonteze, U. Flechsig, S. Rusponi, J. Dreiser, J. Heidler, M. Schmidt, R. Wetter, M. Calvi, T. Schmidt, H. Pruchova, J. Krempasky, C. Quitmann, H. Brune, and F. Nolting, J. Synchrotron Radiat. **19**, 661 (2012).

[47] J. Stöhr and H. C. Siegmann, *Magnetism: From Fundamentals to Nanoscale Dynamics* (Springer, Berlin, Heidelberg, 2006).

[48] A. Uldry, F. Vernay, and B. Delley, Phys. Rev. B **85**, 125133 (2012).

[49] Y. Teramura, A. Tanaka, B. Thole, and T. Jo, J. Phys. Soc. Jpn. **65**, 3056 (1996).

[50] B. T. Thole, G. van der Laan, and G. A. Sawatzky, Phys. Rev. Lett. **55**, 2086 (1985).

[51] J. Dreiser, C. Wäckerlin, M. E. Ali, C. Piamonteze, F. Donati, A. Singha, K. S. Pedersen, S. Rusponi, J. Bendix, P. M. Oppeneer, T. A. Jung, and H. Brune, ACS Nano **8**, 4662 (2014).

[52] G. Kaindl, G. Kalkowski, W. D. Brewer, B. Perscheid, and F. Holtzberg, J. Appl. Phys. **55**, 1910 (1984).

[53] P. Quaino, E. Santos, G. Soldano, and W. Schmickler, Adv. Phys. Chem. **2011**, 1 (2011).

[54] G. Meyer, *Encyclopedia of Inorganic and Bioinorganic Chemistry* (John Wiley & Sons, Köln, 2011).

[55] D. A. Papaconstantopoulos, *Handbook of the Band Structure of Elemental Solids* (Springer, New York, 1985).

[56] B. Hammer and J. K. Nørskov, Adv. Catal. **45**, 71 (2000).

[57] Y. Jia, J. Solid State Chem. **95**, 184 (1991).

[58] N. F. Chilton, D. Collison, E. J. L. McInnes, R. E. P. Winpenny, and A. Soncini, Nat. Commun. **4**, 3551 (2013).
[59] J. J. Baldoví, J. M. Clemente-Juan, E. Coronado, and A. Gaita-Ariño, Inorg. Chem. **53**, 11323 (2014).
[60] J. J. Baldoví, J. J. Borrás-Almenar, J. M. Clemente-Juan, E. Coronado, and A. Gaita-Arino, Dalton Trans. **41**, 13705 (2012).
[61] Y. Shapira, M. T. Liu, S. Foner, R. J. Howard, and W. H. Armstrong, Phys. Rev. B **63**, 094422 (2001).
[62] Y. Shapira, M. T. Liu, S. Foner, C. E. Dubé, and P. J. Bonitatebus, Jr., Phys. Rev. B **59**, 1046 (1999).
[63] A. A. Khajetoorians, T. Schlenk, B. Schweflinghaus, M. dos Santos Dias, M. Steinbrecher, M. Bouhassoune, S. Lounis, J. Wiebe, and R. Wiesendanger, Phys. Rev. Lett. **111**, 157204 (2013).
[64] H. Brune, G. S. Bales, J. Jacobsen, C. Boragno, and K. Kern, Phys. Rev. B **60**, 5991 (1999).
[65] S. Stepanow, A. Mugarza, G. Ceballos, P. Moras, J. C. Cezar, C. Carbone, and P. Gambardella, Phys. Rev. B **82**, 014405 (2010).
[66] F. Meier, L. Zhou, J. Wiebe, and R. Wiesendanger, Science **320**, 82 (2008).
[67] A. A. Khajetoorians, J. Wiebe, B. Chilian, S. Lounis, S. Blügel, and R. Wiesendanger, Nat. Phys. **8**, 497 (2012).
[68] F. Silly, M. Pivetta, M. Ternes, F. Patthey, J. P. Pelz, and W.-D. Schneider, Phys. Rev. Lett. **92**, 016101 (2004).
[69] N. N. Negulyaev, V. S. Stepanyuk, L. Niebergall, P. Bruno, M. Pivetta, M. Ternes, F. Patthey, and W.-D. Schneider, Phys. Rev. Lett. **102**, 246102 (2009).
[70] T. R. Umbach, M. Bernien, C. F. Hermanns, A. Krüger, V. Sessi, I. Fernandez-Torrente, P. Stoll, J. I. Pascual, K. J. Franke, and W. Kuch, Phys. Rev. Lett. **109**, 267207 (2012).
[71] M. Ternes, C. Weber, M. Pivetta, F. Patthey, J. P. Pelz, T. Giamarchi, F. Mila, and W.-D. Schneider, Phys. Rev. Lett. **93**, 146805 (2004).